Microsyst Technol (2011) 17:1037–1049
DOI 10.1007/s00542-011-1288-9

TECHNICAL PAPER

A new two-DOF rotational optical image stabilizer

Paul C.-P. Chao · Yu-Han Chen · Chi-Wei Chiu · Meng-Yen Tsai · Jyh-Yeong Chang · Shir-Kuan Lin

Received: 31 August 2010 / Accepted: 28 March 2011 / Published online: 10 April 2011

Abstract This work proposes design, optimization and validation of a new two degree-of-freedom (DOF) rotational optical image stabilizer (OIS) that is suitable for installing into a mobile-phone-camera. This OIS differs from the previous designs since it stabilizes the lens holder directly by two-DOF translational mechanisms that are actuated by voice coil motors. The work can be divided into three main parts: (1) designs of mechanism and genetic algorithm (GA) optimization of magnetic field, (2) establishments of the dynamic model and equation of motions (EOM) of a dual-axis rotational structure, and (3) realizations of a sliding mode control (SMC) controller with fine performance. The dynamic of the dual-axis rotational OIS system has been analyzed and the EOM has been derived. Based on the Lagrange's method, the motions of the OIS have been modeled through considering kinetic energy and electromagnetic torques. In the last part, the theory of SMC is applied, and the associated simulations are conducted. Based on the simulation results, the SMC controller is forged with the assistances from MATLAB pre-simulation and tested by a microprocessor module. After a series of experiments and verifications, the prototype of the novel OIS is finally accomplished with satisfactory performance of vibration reduction.

P. C.-P. Chao (✉) · Y.-H. Chen · C.-W. Chiu · M.-Y. Tsai · J.-Y. Chang · S.-K. Lin
Department of Electrical Engineering, National Chiao Tung University, Hsinchu 300, Taiwan
e-mail: pchao@mail.nctu.edu.tw

P. C.-P. Chao
Institute of Imaging and Biomedical Phonics, National Chiao Tung University, Tainan 711, Taiwan

1 Introduction

An optical image stabilizer has become an important feature nowadays in a camera, and also mobile phones. Past studies working on two kinds of image stabilizers for compensating the hand-shakings are digital and optical image stabilizers (Ko et al. 1998; Yeom 2009) (DIS and OIS, respectively). However, the development of the DIS was limited by requiring additional buffer memory and compensating hand-shakings and/or shocks with low performance (Chang et al. 2002). This study presents design, optimization and validation of a new two degree-of-freedom (DOF) rotational OIS that is actuated by voice coil motors (VCMs) (Choi et al. 2008). This OIS differs from the previous designs (Yeom 2009; Chiu et al. 2007; Tu et al. 2009; Yu and Liu 2008) that stabilizes the lens holder by two-DOF translational mechanism. As compared to the translational one (Chen et al. 2003; An et al. 1999), the proposed rotational OIS is in small and slim size (only 11 mm × 11 mm × 8 mm) in order to be installed in mobile phones with favorable performance for compensating hand shocks. The dynamic of the OIS has been analyzed in this study and the sliding mode control (SMC) has been applied to realize the controller.

This study is dedicated to construct an OIS system that works against external impulsive excitations. The design and validation of the OIS is completed by three parts of work: (1) optimization of the OIS mechanism and the associated magnetic fields to maximize the actuating torques generated by VCMs; (2) establishment of the associated dynamic governing equations and design of a sliding-mode controller; (3) performance simulation and experimental validation. The effort in the first part is aimed to designing a yoke-less, small-size VCM actuator, which offers the motions of the lens holder in the rotational DOFs

along yaw and pitch directions subjected to maximized magnetic torques. The torque maximization is achieved via the application of genetic algorithm (GA) (Im et al. 2003; Grefenstette 1986) for finding optimum design parameters of VCM components and various sizes. After the goal of optimization is accomplished, the system dynamic equations are next derived based on the Lagrange's method (O'Reilly 2007; De Callafon et al. 2006). The equations of motion (EOM) are derived by considering the variations of the magnetic force, moments of inertia and the rotation angles of the lens module changes, the complicated dynamics of the OIS can be deciphered via equations. With the derived EOMs, the sliding mode control (Chao and Shen 2009; Utkin 1977; Bartolini et al. 2000) is designed and applied for precise angular position and velocity control. Since the EOMs of the system are nonlinear, using the method of a direct nonlinear control is more effective than using a linear control with linearization-EOMs. Besides, the SMC can reduce the tracking errors to zero in finite time. It is found that the controller designed based on the established equations of motion is capable of positioning the lens holder to the desired angles within $\pm 2.5^\circ$ in the required 0.3 s. A series of simulation and experiment are operated in the third part. Finally, the compact OIS is developed. The performance for different types of shock is tested, and the function of image stabilization is therefore proven.

2 Mechanism design and GA optimization

2.1 Mechanism design

The mechanism design of the proposed yoke-less and small size OIS actuator consisted of several parts, the camera lens module unit and a supporting frame attached with VCMs and magnets, etc., which is shown in Fig. 1. This unique OIS owns rotational DOFs along directions of yaw and pitch. Since the structure is designed for implementation in a typical mobile phone, bulky components are out of consideration. Note that the camera lens module unit is suspended from a patterned spring, and a gyroscope is attached under its bottom for sensing shocks/shakings. The module can rotate along two axes to stabilize captured images while subjected to external impulsive vibrations. To generate electro-magnetic forces by VCMs for attenuate these vibrations, two magnets with opposite poles are attached on each sides of a shielding case of the lens module. Slim coils are wound around the inner windows of the frame for carrying VCM currents to move the camera module unit. The total size of this OIS actuator is 11 mm × 11 mm × 8 mm, as shown in Fig. 1b.

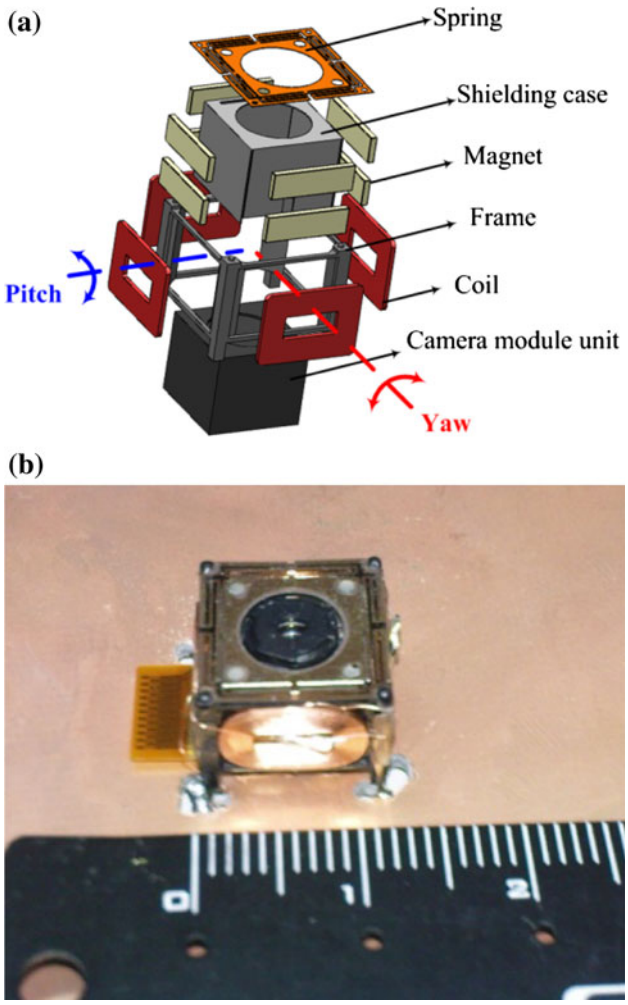

Fig. 1 **a** The blown-up of the proposed magnetic actuator. **b** The manufactured OIS

2.2 Genetic algorithm

To achieve maximum actuation sensitivity with minimizing tilt angle, the well-known genetic algorithm (GA) is employed for finding the optimal parameters in the OIS structure design. The optimization process is similar to that in (Chiu et al. 2007) The optimization aims to consider three perspectives—sensitivity, electro-magnetic torque and power consumption. The sensitivity of the OIS is related to the acceleration

$$A = \frac{F}{M}, \tag{1}$$

where M is the total mass of the camera module, which is around 1 g, including those of the magnets, the lens unit, shielding case, etc. F is the VCM-generated electromagnetic force, which can be expressed as

$$F = N \cdot i \cdot \mathbf{l} \times \mathbf{B_g}, \tag{2}$$

where N is the number of coil loops of a VCM, i is the VCM current, $\mathbf{l}$ is the total length wire, and $\mathbf{B_g}$ is the magnetic flux density that results from geometric design of magnets and shielding case. Herein, a GA algorithm is forged and applied to acquire the optimal results of the VCM-generated electro-magnetic force.

Another important point should be concerned is that the magnetic force induces tilting forces on the lens module due to the relative mis-positionings of the lens module to its housing. Therefore, maximizing the ratio of generating force and the possible tilting force brings out the best performance. With those conditions, the fitness function to maximize for GA can be derived as

$$f_{fitness} \equiv \frac{A}{F_T \cdot P}, \tag{3}$$

where F_T is the tilting torque while P is the consumed power. Since the tilting force in the OIS obeys $F_T = Fr$ where r is the associated moment arm,

$$f_{fitness} = \frac{A}{F_T \cdot P} = \frac{F/M}{FrP} = \frac{1}{rMP}. \tag{3a}$$

Due to the fact that r and M are nearly constants, the defined fitness depends largely on the power consumed.

The settings of the GA algorithm are described as follows: the population is set as 100; the crossover and mutation rates are set as 0.7 and 0.2; the number of generation for optimization is set as 1,000. The different settings of trials had also applied to prove that the results are already converged under the pre-set criterion. Figure 2a shows the evolution of the fitness function values during GA optimization. Table 1 gives the resulted optimal values which are all extremes of their pre-considered ranges, except for l_1 and l_2, the efficient lengths of reluctances of the shielding case and magnets, respectively.

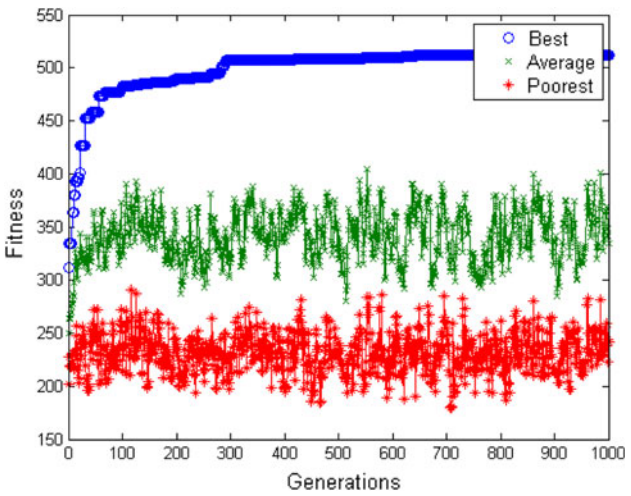

Fig. 2 Results of GA optimization

3 Equations of motion

The dynamic characteristics of the proposed OIS are analyzed in this section, and then the equations of motion (EOMs) would be derived. Considering only rotational dynamics of the lens module, the dynamics can be analyzed through estimating the moments of inertia and the angular velocities of the camera module unit. Based on the Lagrange's equation (Rao 1986), the equations of motion can be derived by

$$\frac{d}{dt}\left(\frac{\partial \mathbf{T}}{\partial \dot{\mathbf{q}}_\mathbf{i}}\right) - \frac{\partial \mathbf{T}}{\partial \mathbf{q}_\mathbf{i}} + \frac{\partial \mathbf{U}}{\partial \mathbf{q}_\mathbf{i}} = \mathbf{Q}_\mathbf{i}, \tag{4}$$

where $\mathbf{T}$ is the matrix of kinetic energy, $\mathbf{U}$ is the matrix of potential energy, $\mathbf{Q_i}$ is a vector of applied torques, and $\mathbf{q_i}$ is the vector of states.

The dynamic of the OIS owns two rotational DOFs. For calculating the kinetic energy, the moments of inertia and angular velocities should be known first. In the mechanical structure, the center of mass (CM) of camera lens module is always at some position when rotating. In other words, the coordinates of the lens CM is unchanged throughout controlling process. The pitch-axis rotates along x-axis while yaw-axis along y-axis. In this nonlinear system, two main parts are to be discussed. One part is about the changes of moments of inertia, while another part is about the variations of electromagnetic torques. In the first part, the variations of moment of inertia are considered. Since the electromagnetic torques are always applied along pitch and yaw-axis, the moment of inertia of the camera module changes with different angular position. Therefore, the term of moment of inertia is incorporates into EOM. In the second part, the variations of electromagnetic torque are discussed. The cause of torque variations is because the magnetic field varies during the rotations of the camera module. The magnetic field is related to the angle of rotations of both pitch and yaw axes.

3.1 Variations of moment of inertia

Define O_{xyz} as a system of ground coordinates whose origin O is at the center of top face of camera module unit, as shown Fig. 3. The moment of inertia for module in motionless situation is easy to be obtained since the camera module is a rectangular solid. Once the dual-axis camera lens module rotates along pitch and yaw-axis, the new moments of inertia should be re-calculated through following procedures. The rotational angles of the camera lens module along pitch and yaw axes with respect to the ground coordinates are define as θ_g and ϕ_g, which can be measured by a gyroscope. On the other hand, the angles of the camera lens module relative to the frame are defined as

Table 1 GA variables and optimal results

Symbol	Range	Definition	Optimal result
l_1	$0.004 \le l_1 \le 0.006$ (m)	As shown below	0.004
l_2	$0.001 \le l_2 \le 0.003$ (m)	As shown below	0.001514
l_m	$0.003 \le l_m \le 0.009$ (m)	As shown below	0.003
d_1	$0.0001 \le d_1 \le 0.0005$ (m)	As shown below	0.0001
d_m	$0.0004 \le d_m \le 0.0007$ (m)	As shown below	0.0004
l_c	$0.02 \le l_c \le 0.03$ (m)	Wire length per loop of a coil	0.02
d_g	$0.0004 \le d_g \le 0.001$ (m)	As shown below	0.00078
N	$100 \le N \le 150$	Loop number of a coil	100

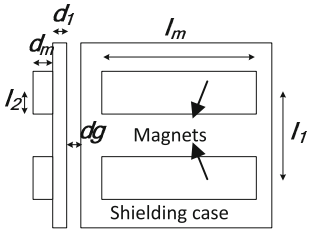

Side View of the OIS

θ_f and ϕ_f, which are shown in Fig. 3. The angular velocities of the camera module, $\dot{\theta}_g$ and $\dot{\phi}_g$, can be expressed as

$$\dot{\theta}_g = \int \frac{\tau_{disturb-p}}{I_{total-p}} dt + \dot{\theta}_f, \qquad \dot{\phi}_g = \int \frac{\tau_{disturb-y}}{I_{total-y}} dt + \dot{\phi}_f, \tag{5}$$

where $\tau_{disturb-p}$ and $\tau_{disturb-y}$ are the torques caused by shocks/disturbances, and $I_{total-p}$ and $I_{total-y}$ are the total inertias of the OIS along pitch and yaw axes, respectively. The kinetic energy of the camera lens module with respect to the frame with the conditions $\theta_f = \phi_f = 0$ can be calculated with known angular velocities along two axes, which are

$$\omega_{pitch} = \dot{\theta}_g, \qquad \omega_{yaw} = \dot{\phi}_g. \tag{6}$$

The kinetic energy becomes

$$T = \frac{1}{2}(I_x \dot{\theta}_g^2 + I_y \dot{\phi}_g^2 - I_{xy}\dot{\theta}_g\dot{\phi}_g - I_{yx}\dot{\theta}_g\dot{\phi}_g), \qquad I_{xy} = I_{yx} = 0, \tag{7}$$

where I_x and I_y are the moments of inertia of the module with respect to x and y axes. I_{xy} and I_{yx} denote the cross moments of inertia. Nevertheless, when the angle between frame and camera unit is not zero, the moments of inertia change. In other words, when θ_f and ϕ_f vary with nonzero values, the equations need to be revised. Having rotated x axis by θ_f and y axis by ϕ_f with respect to frame and based on Fig. 3, the rotation matrices corresponding to x-axis and y-axis are (Boresi and Schmidt 2001)

$$R_x(\theta_f) = \begin{bmatrix} 1 & 0 & 0 \\ 0 & \cos\theta_f & \sin\theta_f \\ 0 & -\sin\theta_f & \cos\theta_f \end{bmatrix} \tag{8}$$

and

$$R_y(\phi_f) = \begin{bmatrix} \cos\phi_f & 0 & -\sin\phi_f \\ 0 & 1 & 0 \\ \sin\phi_f & 0 & \cos\phi_f \end{bmatrix}. \tag{9}$$

Therefore, the new vector after rotation along both non-zero pitch(x) and yaw(y) axes of the inner lens module can be obtained by the rotation matrix

$$R_x(\theta_f)R_y(\phi_f) = \begin{bmatrix} \cos\phi_f & 0 & -\sin\phi_f \\ \sin\theta_f\sin\phi_f & \cos\theta_f & \sin\theta_f\cos\phi_f \\ \sin\phi_f\cos\theta_f & -\sin\theta_f & \cos\theta_f\cos\phi_f \end{bmatrix}.. \tag{10}$$

Using the above rotation matrix, the moments of inertia of the camera lens module in rotations with respect to frame can be found, which are

$$I_{pitch} = I_x\cos^2\phi_f + I_y\sin^2\theta_f\sin^2\phi_f + I_z\sin^2\phi_f\cos^2\theta_f, \qquad I_{yaw} = I_y\cos^2\theta_f + I_z\sin^2\theta_f. \tag{11}$$

The above resulted inertias have been confirmed by comparing the values with those obtained from software. The results of numerical and simulation are the same,

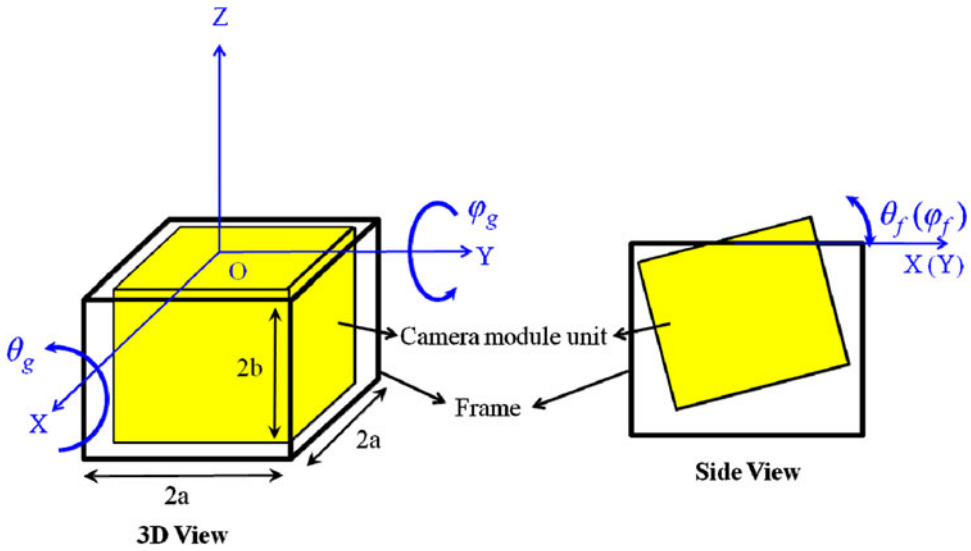

Fig. 3 The coordinates and parameters of the camera module

therefore, the equations are shown effectiveness. Then, the kinetic energy can be derived as

$$T = \frac{1}{2}(I_x \cos^2\phi_f + I_y \sin^2\theta_f \sin^2\phi_f + I_z \sin^2\phi_f \cos^2\theta_f)\dot{\theta}_f^2 + \frac{1}{2}(I_y \cos^2\theta_f + I_z \sin^2\theta_f)\dot{\phi}_f^2. \tag{12}$$

On the other hand, the potential energy of this system is assumed zero. That is

$$\frac{\partial U}{\partial q_1} = \frac{\partial U}{\partial q_2} = 0. \tag{13}$$

Therefore, Eq. 4 can be expressed as

$$\begin{aligned}&(I_x \cos^2\phi_f + I_y \sin^2\theta_f \sin^2\phi_f + I_z \sin^2\phi_f \cos^2\theta_f)\ddot{\theta}_f \\ &\quad - (I_y \sin\theta_f \cos\theta_f \sin^2\phi_f - I_z \sin\theta_f \cos\theta_f \sin^2\phi_f)\dot{\theta}_f^2 \\ &\quad - (-I_y \sin\theta_f \cos\theta_f + I_z \sin\theta_f \cos\theta_f)\dot{\phi}_f^2 \\ &= Q_1 = \tau_{pitch} - k_p\theta_f\end{aligned} \tag{14}$$

and

$$\begin{aligned}&(I_y \cos^2\theta_f + I_z \sin^2\theta_f)\ddot{\phi}_f \\ &\quad - (-I_x \sin\phi_f \cos\phi_f + I_y \sin^2\theta_f \sin\phi_f \cos\phi_f \\ &\quad + I_z \sin\phi_f \cos\phi_f \cos^2\theta_f)\dot{\theta}_f^2 \\ &= Q_2 = \tau_{yaw} - k_y\phi_f,\end{aligned} \tag{15}$$

where Q_1 and Q_2 result from VCM torques; τ_{pitch} and τ_{yaw} are electromagnetic torques of pitch and yaw, and k_p and k_y are stiffness constants of sheet springs as shown in Fig. 1a. Note that τ_{pitch} and τ_{yaw} vary with different angles of rotation. The spring sizes are determined to render an acceptable balance between high DC sensitivity and adequate bandwidth offered by this OIS driver (Chiu et al. 2007). The equation of torques along two axes will be discussed in the next section.

3.2 Variations of electromagnetic torque

Another characteristic of the nonlinear OIS system is the variations of the electromagnetic torque. The causes of the variations are twofold. One is the distance between coils and magnets and another is the vector of the magnetic field. It is obvious that the different angles of rotation would result in various dynamics. To analyze the variations of torque, several assumptions are set up: (1) the magnetic field of the coils is almost uniform (i.e. no large magnetic field difference between the center and the edge of magnets). With this assumption, the distance and the normal vector of magnets are the only things needed to be concerned and (2) the position of central point of the lens is invariable during the rotation.

With these assumptions, the simulation model using Maxwell 11 is built. The simulation range of angle is from $-3°$ to $3°$ for rotating both pitch (θ_f) and yaw-axis (ϕ_f). Based on the simulation data and electromagnetic theory, the electro-magnetic torques applied to the lens module can be calculated by a numerical method. The magnets are the major design factor and the original magnetic force generated by VCM coils and magnets without rotations is assumed as $F_0 = N \cdot i \cdot \mathbf{l} \times \mathbf{B_0}$, where F_0 is the generated force while $\mathbf{B_0}$ is the original magnetic field vector. Since the magnitude of magnetic force is in inversely proportional to square of distance between coils and magnets, the distance with rotations should be considered. The VCM driving torque can be obtained by calculating the electro-magnetic force and spring force at each facet of the lens module. The equation of the torque τ is then

$$\tau_{pitch} = a\cos^2\phi_f F_0\left(\frac{d_0^2((d_0+a(1-\cos\phi_f)^2+b^2\sin^2\phi_f)}{((d_0+a(1-\cos\phi_f))^2-b^2\sin^2\phi_f)^2}\right),$$
$$\tau_{yaw} = a\cos^2\theta_f F_0\left(\frac{d_0^2((d_0+a(1-\cos\theta_f)^2+b^2\sin^2\theta_f}{((d_0+a(1-\cos\theta_f))^2-b^2\sin^2\theta_f)^2}\right), \quad (16)$$

where d_0 is the initial distance between coils and magnets (i.e. $\theta_f = \phi_f = 0$). a and b are the geometric parameters as shown in Fig. 3. Therefore, the two complete EOM with respect to pitch and yaw axes are next derived, and all of the states have become

$$\begin{bmatrix}\dot\theta_f\\ \ddot\theta_f\\ \dot\phi_f\\ \ddot\phi_f\end{bmatrix} = \begin{bmatrix}\dot\theta_f\\ f_1(\theta_f,\dot\theta_f,\phi_f,\dot\phi_f)+g_1(\theta_f,\dot\theta_f,\phi_f,\dot\phi_f)u_1\\ \dot\phi\\ f_2(\theta_f,\dot\theta_f,\phi_f,\dot\phi_f)+g_2(\theta_f,\dot\theta_f,\phi_f,\dot\phi_f)u_2\end{bmatrix},$$
$$u_1 = i_{pitch}\ and\ u_2 = i_{yaw}, \quad (17)$$

where f_1, f_2, g_1, and g_2 are nonlinear functions used to represent the terms derived above, while u_1 and u_2 are input currents. Figure 4 shows the block diagram of the stabilizer system, controller and their input/output variables.

4 Sliding mode control

The sliding mode controller (SMC) is able to eliminate the state tracking errors in finite time, and is applicable to a system with nonlinear dynamic. Therefore, the control of the actuator is accomplished by SMC. The application of the sliding mode control for the OIS system is described in this section, while Fig. 4 illustrates the control scheme by a block diagram.

The first step of designing a sliding mode control second-order system is to derive a nonlinear equation in the canonical form:

$$\ddot x = f(\mathbf{x}) + g(\mathbf{x})u, \quad (18)$$

where $\mathbf{x}$ is the output of interest (i.e. the angular positions and velocities of pitch and yaw), and u is the control input (i.e. the input current for controlling the electromagnetic torque). The function $f(\mathbf{x})$ is nonlinear and has to be upper bounded by a continuous function of x. $g(\mathbf{x})$ is also a nonlinear function that is multiplied by the input u. The function f is not always known. If the f is undetermined, it can be estimated as $\hat f$. The estimation error on f is assumed to be bounded by some known function F as

$$\left|\hat f - f\right| \le F. \quad (19)$$

Fortunately, the function f is already derived in the previous section, thus, the equation exists, and the estimated error is out of consideration. For achieving the sliding mode control, the input u and the sliding surface s is next determined in the following equations,

$$g\hat u_i = -f_i + \ddot x - \lambda\dot{\tilde x}$$
$$u_i = \hat u_i - k\,\mathrm{sgn}(s)$$
$$= (-f_i + \ddot x - \lambda\dot{\tilde x})/g - k\,\mathrm{sgn}(s), \quad i = 1,2, \quad (20)$$

and

$$s = \dot{\tilde x} + \lambda\tilde x = (\dot x - \dot x_d) + \lambda(x - x_d), \quad (21)$$

where k is a proper scale that be chose, λ is a strictly positive constant, sgn(.) is the sign function, and x_d is the desired sate. More specifically, the goal of the control is to stabilize the camera module with respect to ground (i.e. $\theta_g = \dot\theta_g = \phi_g = \dot\phi_g = 0$). Thus, the desired states can be expressed as

$$\theta_{fd} = \theta_g - \theta_t,$$
$$\phi_{fd} = \phi_g - \phi_t,$$
$$\dot\theta_{fd} = \dot\theta_g - \dot\theta_t,$$
$$\dot\phi_{fd} = \dot\phi_g - \dot\phi_t, \quad (22)$$

where $\{\theta_t, \phi_t, \dot\theta_t, \dot\phi_t.\}$ prescribes the angular motions of the frame which is caused by external disturbances, which can be sensed by a gyroscope in an on-line fashion.

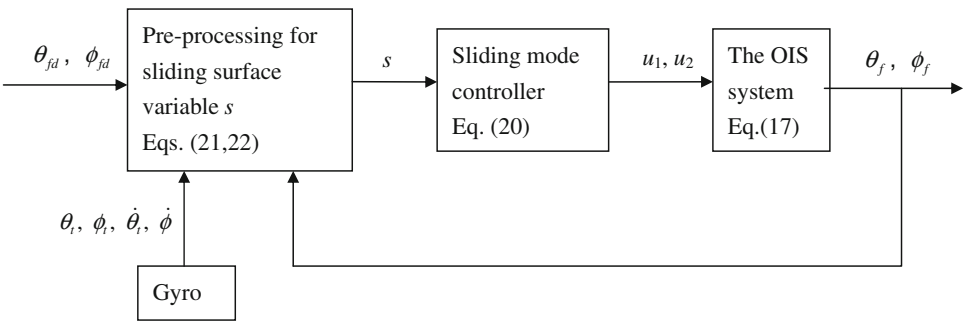

Fig. 4 The blocks for the stabilizer system and controller

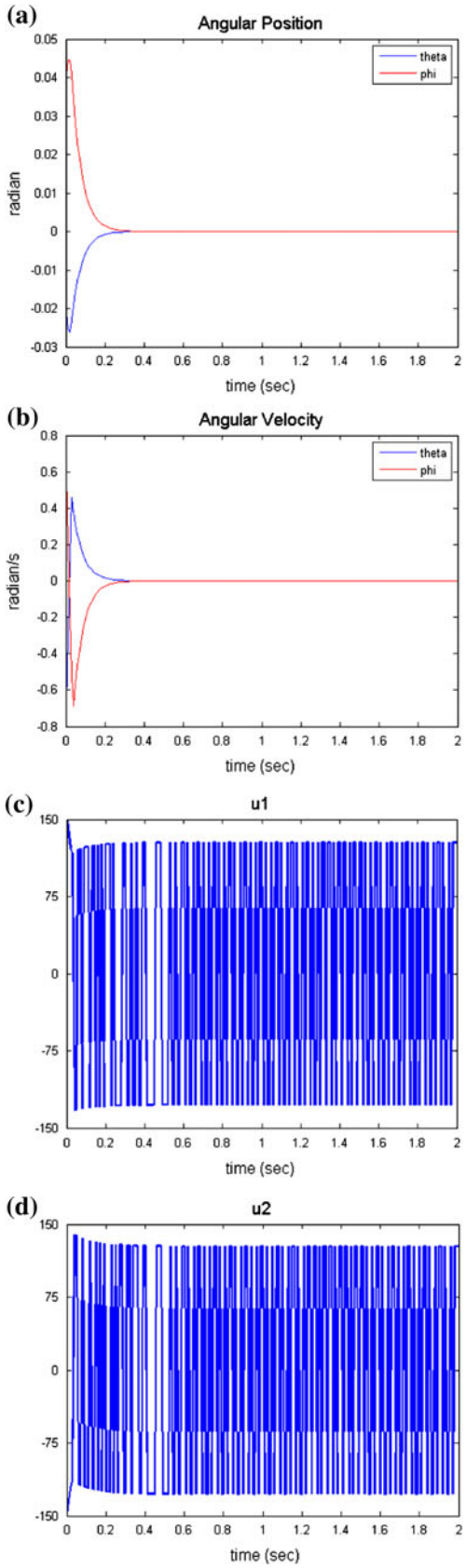

Fig. 5 **a** Simulation results of angular positions; **b** angular velocities; **c** input u_1; **d** input u_2

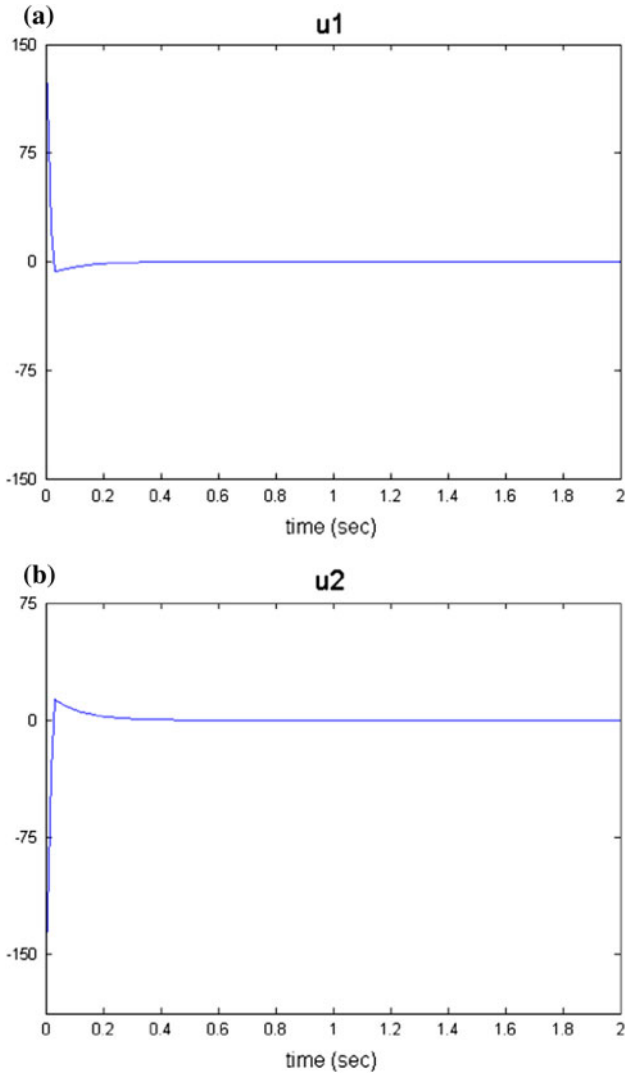

Fig. 6 **a** The simulation result of u_1 with the revised control law; **b** u_2 with the revised control law

In general, the chattering is a serious problem of SMC, and should be eliminated. This can be achieved by revising the control law with a thin boundary layer neighboring the switching surface

$$B(t) = \{\mathbf{x}, |s(\mathbf{x};t)| \leq \Phi\} \quad \Phi > 0, \tag{23}$$

where Φ is the thickness of boundary layer, and $\varepsilon = \Phi/\lambda^{n-1}$ is the boundary width. In other word, revise the control input with a boundary layer

$$u = \hat{u} - k\ \mathrm{sat}(s/\Phi). \tag{24}$$

By this way, the control law u becomes continuous, and was chosen as before outside of B(t). Finally, the sliding mode control of the dual-axis system can be realized by controlling the input current. Two factors of controller, u_1 and u_2, can be derived by solving Eq. 20. Since the compensate range is between $\pm 2.5°$. For simulation,

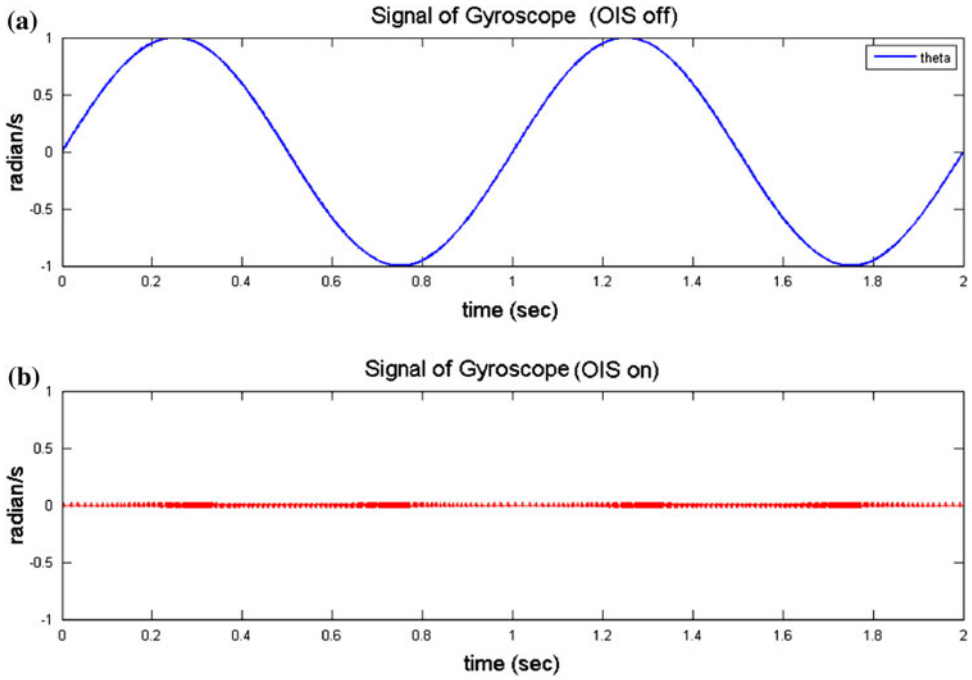

Fig. 7 **a** The assumed shock signal; **b** The compensated shock signal of Case 1

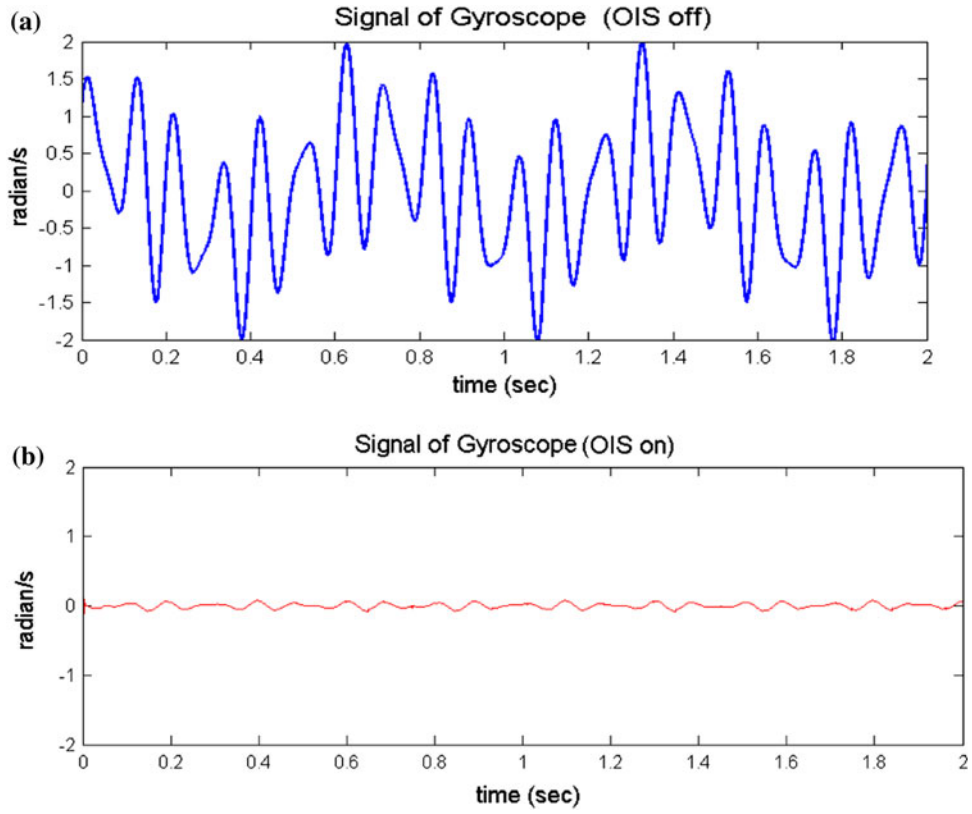

Fig. 8 **a** The assumed shock signal; **b** The compensated shock signal of Case 2

consider a case with initial conditions $\theta_g = -0.02$, $\phi_g = 0.04$ (radian), $\dot{\theta}_g = -0.8$ and $\dot{\phi}_g = 0.7$ (rad/s), and the simulation results are shown in Fig. 5a–d. The settling time is <0.15 s. Another case (Case 2) is simulated with the revised control laws. The simulation results are shown as Fig. 6a and b. Obviously, the inputs u_1 and u_2 are smooth now, and this is helpful to overcome the problems of chattering.

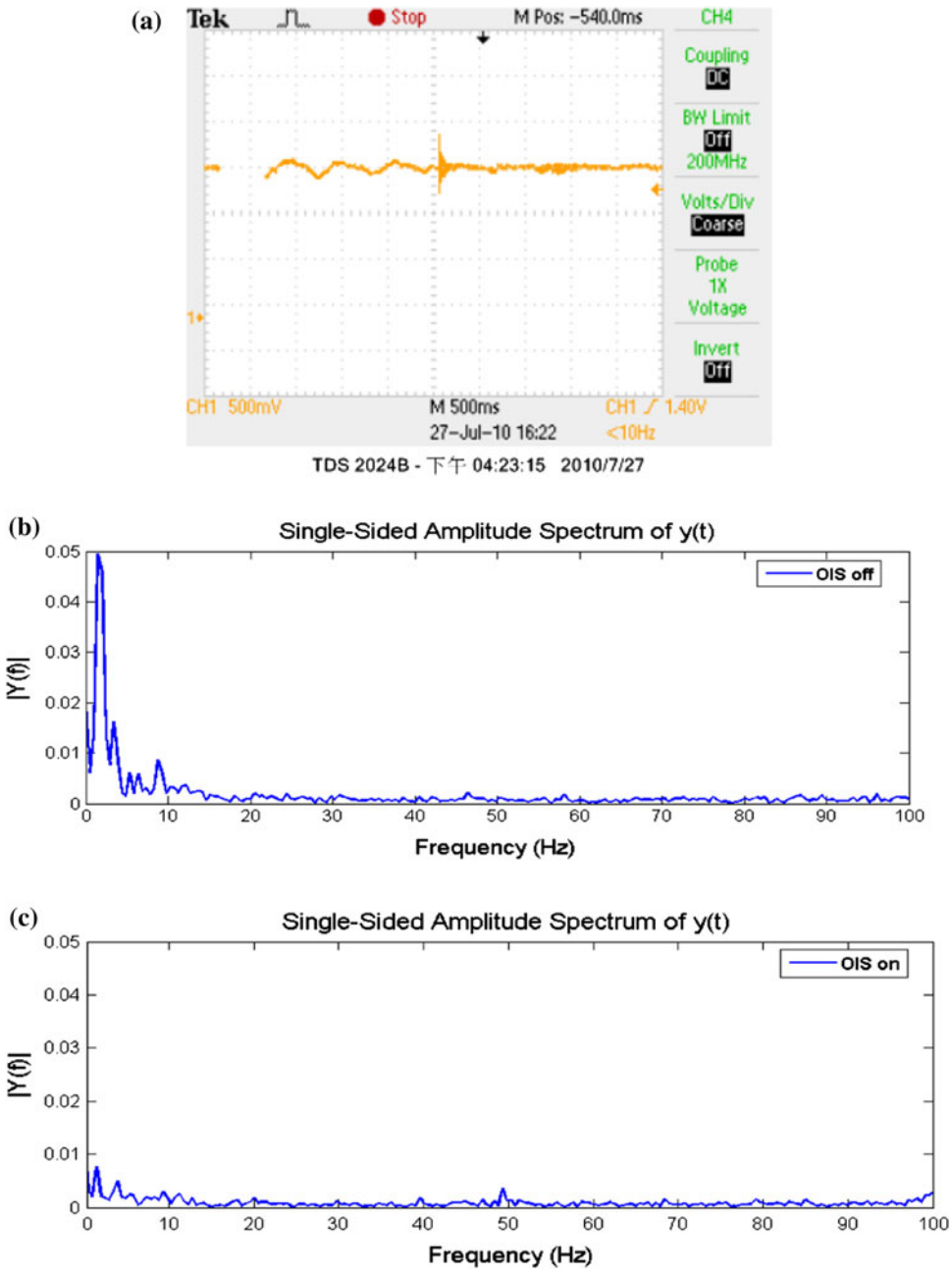

Fig. 9 **a** The OIS off/on signals for Case A measured by oscilloscope. **b** The OIS-off FFT results of the practical shock signal. **c** The OIS-on FFT results of the practical shock signal

5 Simulation and experimental results

5.1 Simulations for compensating assumed shocks

Since the control law is verified, two simulation cases for compensating assumed shocks are implemented in the next step. The states of angular position and acceleration can be obtained with differentiation and integration. Since shock signals are sensed by a gyroscope, an assumed angular-velocity shock signal is introduced. Two important points are explained here; first, all cases take pitch axis for the example, and the control results along yaw axis could be obtained with the same method; second, the controller works only when someone turns on the OIS. The results of OIS on/off are obtained by the simulation software. Here, the results of two simulation cases (Case 1, 2) are discussed and explained. Case 1, a 10 Hz sine wave with ± 1 rad/s magnitude is applied as a shock signal, as shown in Fig. 7a. Compensated by the controller, the absolute value of shock magnitude is reduced to only 3.5% of the original, as shown as Fig. 7b. Case 2 is simulated by applying sine/cosine combined waves. This angular-velocity shock signals are 1.5, 10, 14 Hz waves, as shown in Fig. 8a. After the compensation, all magnitudes of the shocks with different frequencies have been reduced. The absolute value of the compensated magnitude is reduced to 3.97% with

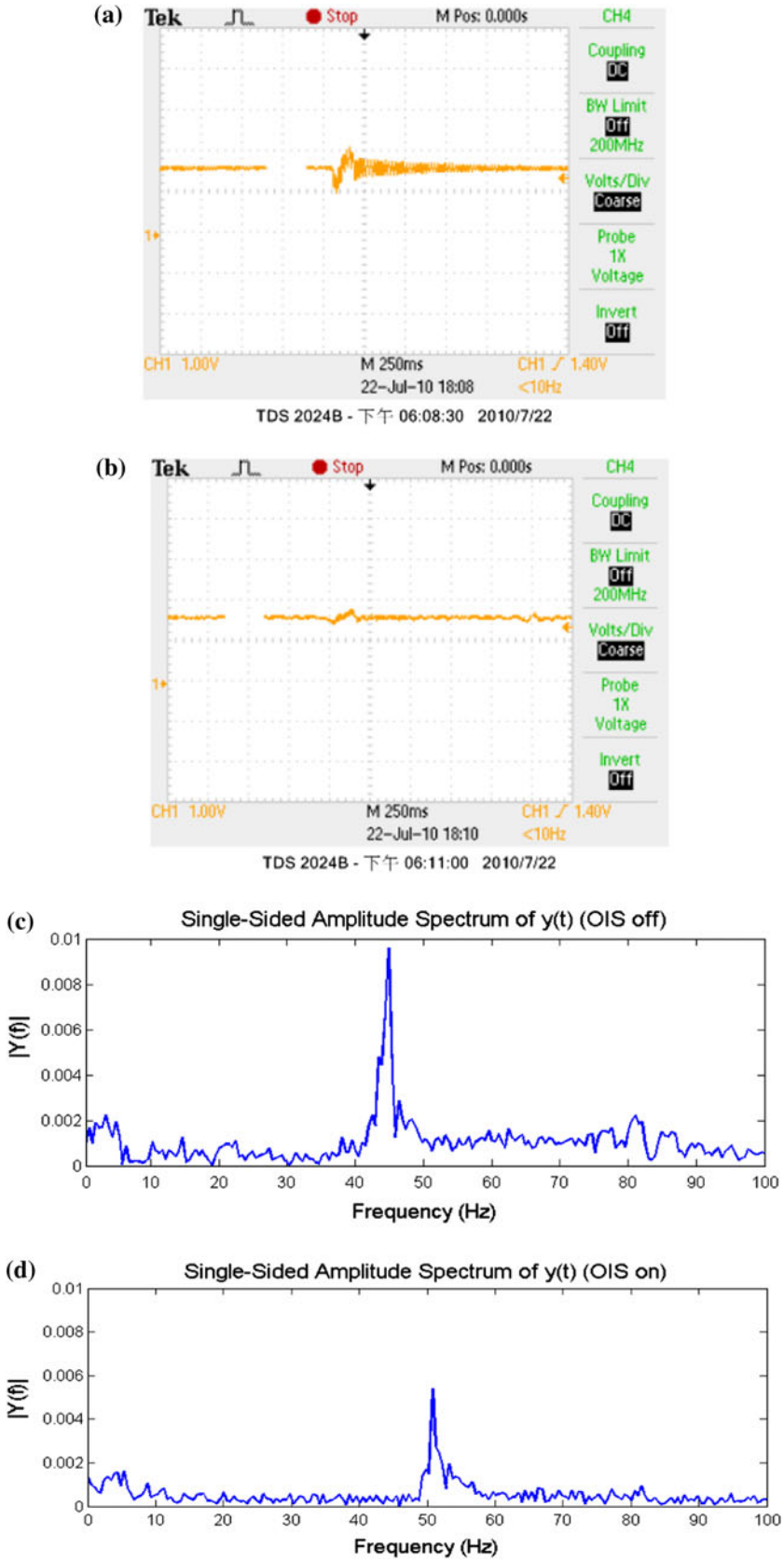

Fig. 10 **a** The OIS-off signals for Case B measured by oscilloscope; **b** The OIS-on signals; **c** The OIS-off FFT results of the practical shock signal. **d** The OIS-on FFT results of the practical shock signal

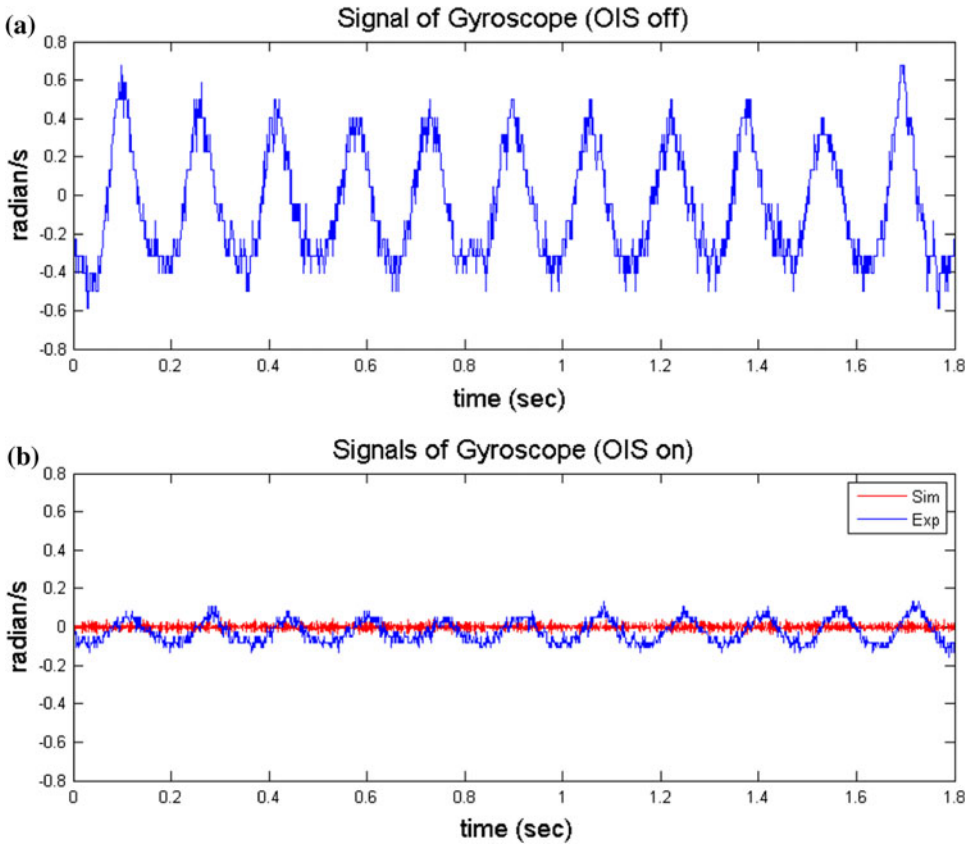

Fig. 11 **a** The gyro signals as OIS being off and under the practical continuous shock. **b** The compensated results of simulation and experiment

respect to the original one, as shown in Fig. 8b. Therefore, these two simulation cases can prove the performance of the controller for compensating random shocks. Thus, the performance of the OIS controller has been proven. With those positive results, the experiments are next operated.

5.2 Experimental results

Two experimental cases (Case A, B) are conducted to test the performance of compensation. Since the continuous shocks occur during users are recording video, a practical continuous hand-shock signal, Case A is therefore tested for confirming the performance. Normally, the shock frequencies of hand shake are lower than 20 Hz. The frequency of shocks in Case A is about 2 Hz, as show in Fig. 9a. The results show that the magnitude of Case A has been reduced to 16.83% of the original after the OIS is turned on, as shown in Fig. 9a. The FFT results are shown in Fig. 9b and c. Another case, Case B, considers a practical hand-shock when someone is pressing the camera shutter button. The signals of OIS off/on are shown in Fig. 10a and b. The magnitude of the shock is reduced to 29.95% of the original after the OIS is turned on. The FFT results are shown in Fig. 10c and d. Therefore, the performance of the manufactured OIS is confirmed.

5.3 Comparison between experiments and simulations

To estimate the errors between simulations and experiments, shock signals are applied in both simulation and experiment. An applied continuous signal is shown in Fig. 11a. The compensated results of simulation and experiment are shown in Fig. 11b. The absolute value of the shock magnitude is reduced to 6.1% by simulation and 17.23% by experiment. Fig. 12a illustrates the shock case that someone is pressing the shutter bottom. The compensated results of simulation and experiment are shown in Fig. 12b. The absolute value of the shock magnitude is reduced to 10.1% by simulation and 29.95% by experiment. With the similar results of simulations and experiments, the prototype of the OIS is proven well designed and the function of image stabilized is demonstrated.

6 Conclusions

A compact OIS is designed and fabricated as a novel design that compensates external shocks by the two DOF rotational mechanism. This design owns the capability to stabilize the lens holder along pitch and yaw axes, and has a wide range of compensation. With a small and slim size

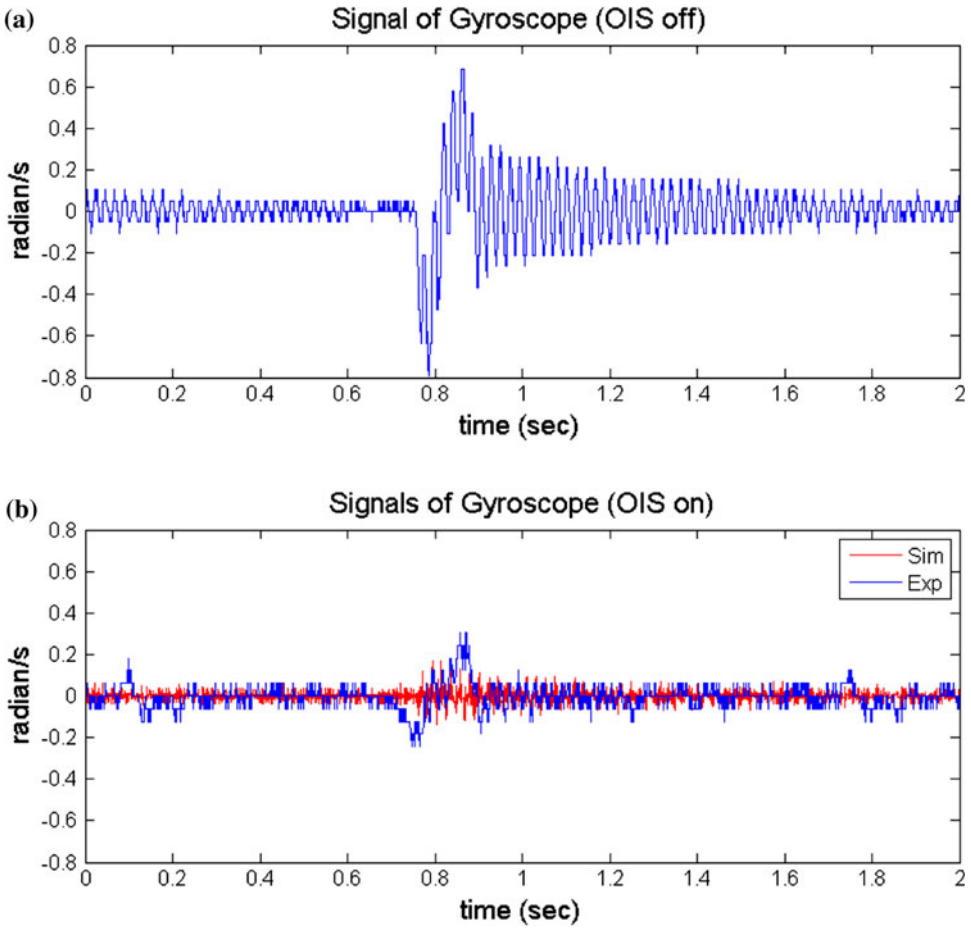

Fig. 12 **a** The gyro signals as OIS being off and under the shock when pressing shutter button. **b** The compensated results from simulation and experiment

(11 mm × 11 mm × 8 mm), this OIS system is suitable for being installed in a mobile phones. Once the OIS is installed in a mobile phone and becomes a standard component, it would be an obvious progress for mobile phone commercialization. This study has accomplished several goals—mechanical design, GA optimization, dynamic analysis, and controller designs. A prototype of the OIS system is built and tested. The shock magnitudes on the lens holder have been reduced to <30% after turning on the OIS.

Since the performance of the OIS is successfully shown by this study, the installation of the OIS into a mobile phone is the next goal to pursue. When the OIS system is turned on, the influences and interactions with other components of mobile should be concerned. Moreover, the research works for more effective controllers, durable mechanisms, and lower power consumption systems will be conducted.

Acknowledgments The authors are also indebted to the National Science Council of R. O. C. for the financial support through the contacts NSC 98-2220-E-009-018- and NSC 98-2622-E-009-006-CC1. The authors are also grateful to National Chip Implementation Center (CIC) of Taiwan for help implement the controllers. This work was supported in part by the UST-UCSD International Center of Excellence in Advanced Bio-engineering sponsored by the Taiwan National Science Council I-RiCE Program under Grant Number: NSC-99-2911-I-010-101.

References

An A, Oh Y, Choi S, Song C (1999) Dual-axis microgyroscope with closed-loop detection. Sens Actuat A 73:1–6

Bartolini G, Ferrara A, Usai E, Utkin VI (2000) On multi-input second order sliding mode control. IEEE Trans Autom Control 45(9):1711–1717

Boresi AP, Schmidt RJ (2001) Engineering mechanics: dynamics. Brooks/Cole Thompson Learning, Pacific Rove

Chang J-Y, Hu W-F, Cheng M-H, Chang B-S (2002) Digital image translational and rotational motion stabilization using optical flow technique. IEEE Trans Consumer Electron 48(1):108–115

Chao PC-P, Shen C-Y (2009) Sensorless tilt compensation for a three-axis optical pickup using a sliding-mode controller equipped with a sliding-mode observer. IEEE Trans Control Syst Technol 17(2):267–282

Chen M-Y, Wang M-J, Fu L-C (2003) A novel dual-axis repulsive maglev guiding system with permanent magnet: modeling and controller design. IEEE Trans Mechatron 8(1)

Chiu C-W, Chao PC-P, Wu D-Y (2007) Optimal design of magnetically actuated optical image stabilizer mechanism for cameras in mobile phones via genetic algorithm. IEEE Trans Magn 43(6):2582–2584

Choi H, Kim J-P, Song M-G, Kim W-C, Park N-C, Park Y-P, Park K-S (2008) Effects of motion of an imaging system and optical image stabilizer on the modulation transfer function. Opt Express 16(25):8

De Callafon RA, Nagamune R, Horowitz R (2006) Robust dynamic modeling and control of dual-stage actuators. IEEE Trans Magn 42(2):247–254

Grefenstette JJ (1986) Optimization of control parameters for genetic algorithms. IEEE Trans Syst Man Cybern 16(1):122–128

Im C-H, Jung H-K, Kim Y-J (2003) Hybrid genetic algorithm for electromagnetic topology optimization. IEEE Trans Magnet 39(5):2163–2169

Ko S-J, Lee S-H, Lee K-H (1998) Digital image stabilizing algorithms based on bit-plane matching. IEEE Trans Consumer Electron 44(3):617–622

O'Reilly M (2007) The dual Euler basis: constraints, potentials, and Lagrange's equations in rigid-body dynamics. ASME J Appl Mech 74:256–258

Rao SS (1986) Mechanical vibration. Addison-Wesley, Reading

Tu T-Y, Chao PC-P, Chiu C-W, Huang J-S, Wang C-C (2009) Fuzzy control design of a magnetically-actuated optical image stabilizer with hysteresis compensation. J Appl Phys 105(7):07F124–07F124-3

Utkin VI (1977) Variable structure systems with sliding mode. IEEE Trans Autom Control 22(2):212–222

Yeom DH (2009) Optical image stabilizer for digital photographing apparatus. IEEE Trans Consumer Electron 55(3):1028–1031

Yu HC, Liu TS (2008) Adaptive model-following control for slim voice coil motor type optical image stabilization actuator. J Appl Phys 103:07F114-1–07F114-3